

Magnetic Behavior of Trigonal (Bi-)pyramidal $3d^8$ Mononuclear Nanomagnets: The Case of $[\text{Ni}(\text{MDABCO})_2\text{Cl}_3]\text{ClO}_4$

Miroslav Georgiev* and Hassan Chamati*

Cite This: *ACS Omega* 2023, 8, 28640–28650

Read Online

ACCESS |



Metrics & More

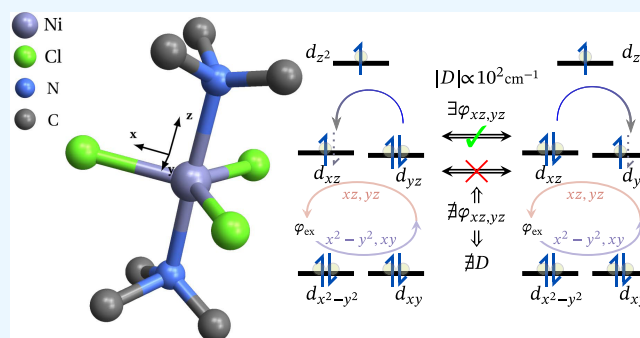


Article Recommendations



Supporting Information

ABSTRACT: This paper attempts to shed light on the origin of the magnetic behavior specific to trigonal bi- and pyramidal $3d^8$ mono- and polynuclear nanomagnets. The focus lies on entirely unraveling the system's intrinsic microscopic mechanisms and fundamental quantum mechanical relations governing the underlying electron dynamics. To this end, we develop a self-consistent approach to characterize, in great detail, all electron correlations and the ensuing fine structure of the energy spectra of a broad class of $3d^8$ systems. The mathematical framework is based on the multiconfigurational self-consistent field method and is devised to account for prospective quantum mechanical constraints that may confine the electron orbital dynamics while preserving the properties of all measurable quantities. We successfully characterize



the experimentally observed magnetic anisotropy properties of a slightly distorted trigonal bipyramidal Ni^{2+} coordination complex, demonstrating that such compounds do not exhibit intrinsic huge zero-field splitting and inherent giant magnetic anisotropy. We reproduce qualitatively and quantitatively the behavior of the low-field magnetic susceptibility, magnetization, low-, and high-field electron paramagnetic resonance spectroscopy measurements and provide an in-depth analysis of the obtained results.

I. INTRODUCTION

Being quantum in nature and standing as promising candidates for the assembly of future molecule-based information density storage devices, mono- and polynuclear molecular magnets have attracted enormous attention in recent decades.^{1–7} Gaining useful knowledge on the quantum dynamics of nonsinglet paired electrons under the action of a particular crystal field (CF), however, may be a great challenge to their theoretical characterization as well as technological applications.

The magnetic properties of transition-metal-based molecular and single-ion magnets are tightly related to the local coordination of metal ions. In general, the CF environment shaped by the bond lengths, type of ligands, coordination number, and geometric symmetry is the main precursor to a particular fine structure related to the ground state (FSG) resulting from the spin–orbit (SO) coupling.^{3,8–11} There exists, however, an additional characteristic behind the distinct magnetic behavior among the metal ions belonging to the same row of the periodic system of elements, that is, the extent of valence subshell occupancy influencing quantitatively the effect of CF and SO coupling on the fine structure (FS) due to Pauli's principle. In that respect, the high-spin $3d^8$ coordination complexes and their ensuing polynuclear nanomagnets^{12–17} are of particular interest, since at a given coordination, they tend to show an unusual magnetic anisotropy (MA). Peculiar cases of mononuclear Ni^{2+} nanomagnets that challenge the current understanding of $3d^8$ -based systems' magnetic behavior are

those possessing either a trigonal bi- or a pyramidal CF.^{18–23} It is essential to point out that in any other CF environment, the magnetic properties of Ni^{2+} complexes are reasonably well understood within the framework of the conventional approach that considers the unpaired electrons as unconstrained. For instance, they are magnetically isotropic in the case of octahedral coordination.^{19,21,24,25} In a distorted or pseudo-octahedral and trigonal prismatic CF, the same complexes exhibit a negligible to a very small SO coupling and hence vanishing FSG.^{26,27} The occurrence of moderate zero-field splitting (ZFS) is also possible as it is demonstrated by the structural dependence in a series of trigonal prismatic Ni^{2+} complexes.²⁸ Moreover, a small to moderate ZFS is observed in the pseudotetrahedral nickel complex,²⁹ hepta-coordinated,³⁰ and the hexacoordinated one.³¹ The occurrence of moderate to large energy gaps in FSG is highly unexpected yet detectable. A prominent example is FSG rising in the pentacoordinated environment^{32,33} and the tetrahedral one.³⁴ ZFS of such a scale may be unexpected, but it is not forbidden by conservation laws or indistinguishability

Received: May 9, 2023

Accepted: June 30, 2023

Published: July 21, 2023



principles. This, however, is not the case for the high-spin trigonal bi- and pyramidal Ni^{2+} complexes as we mentioned earlier and this is what makes the magnetic properties of such systems look puzzling in the framework of the conventional approach.

In general, under the action of strong CF, the calculated probability of observing a very large to huge ZFS in high-spin trigonal bi- and pyramidal Ni^{2+} complexes equals zero since SO coupling between active and core orbitals is forbidden by virtue of Pauli's exclusion principle.²⁵ This is particularly true for the conventional methods since they consider the orbital phases of the electrons as independent variables over infinite time. In the last decade, however, very insightful studies have been reported, showing that a nontrivial FSG indeed exists thus raising the question about its origin. A nontrivial FSG is observed in the low-symmetry trigonal bipyramidal complexes $[\text{Ni}(\text{Me}_6\text{tren})\text{Cl}]\text{ClO}_4$ and $[\text{Ni}(\text{Me}_6\text{tren})\text{Br}]\text{Br}$.³⁵ It was pointed out that the former complex is characterized by an axial ZFS parameter, with a magnitude of about 120 cm^{-1} . The existence of very large energy gaps related to the ground state is, furthermore, reported in ref 36 for the trigonal pyramidal compound $\text{K}\{\text{Ni}(\text{N}[\text{CH}_2\text{C}(\text{O})\text{NC}(\text{CH}_3)_3]_3)\}$ exhibiting high anisotropy. Another prominent case of an unusually large MA is observed in the distorted trigonal bipyramidal complex $[\text{Ni}(\text{MDABCO})_2\text{Cl}_3]\text{ClO}_4$,³⁷ with calculations suggesting a huge magnitude of the axial ZFS parameter of about 535 cm^{-1} . Lately, revisiting the magnetic properties of the complexes $[\text{Ni}(\text{Me}_6\text{tren})\text{X}]$ ($\text{X} = \text{Cl}, \text{Br}$) within the mathematical framework of a superposition model underlined the need for deeper research that may shed light on the origin of ZFS.³⁸ Other studies, such as the far infrared measurements carried out on the species $[\text{Ni}(\text{Me}_6\text{tren})\text{Cl}]\text{ClO}_4$,³⁹ confirming the presence of a large, but not huge, energy gap in FSG and the simulated magnetostructural dependencies in $[\text{Ni}(\text{MeDABCO})_2\text{Cl}_3]\text{ClO}_4$ under high pressure⁴⁰ are important cases emphasizing on the need of in-depth analysis on the nature of ZFS and the genuine origin of MA.

The experimentally observed FSG in the above-mentioned cases definitely points out that unveiling the mechanism underlying the magnetic behavior of Ni^{2+} -based single-ion magnets with trigonal bi- and pyramidal local coordinations cannot be worked out within the conventional parameterization scheme embedded in the effective single-ion Hamiltonians.^{41–44} In other words, SO interactions alone cannot lead to large splitting in FS, and thus, an auxiliary microscopic mechanism underlying the relevant coupling is worth considering. Such an assumption suggests that the electron dynamics of the metal ions of highly filled subshells may be governed by additional rules, more specifically, quantum mechanical constraints that abide by the principle of indistinguishability and hence preserve the exchange symmetry. To the best of our knowledge, a study of the effect of constraining the electron orbital degrees of freedom related to FS of coordination complexes and molecular magnets in general has not been undertaken so far.

The main goal of the present paper is to identify potential quantum constraints that give rise to a unique FSG in Ni^{2+} trigonal bi- and pyramidal coordination complexes. The uniqueness is determined by all constraints that confine the electron orbital dynamics, preserving all relevant observables invariant. To this end, we make use of the exact diagonalization technique developed in ref 45 to characterize $3d^2$ systems and later extended to explore the properties of $3d^8$ -based²⁵ mononuclear nanomagnets. This very approach will be used to explore the unusual magnetic behavior of the compound

$[\text{Ni}(\text{MDABCO})_2\text{Cl}_3]\text{ClO}_4$,³⁷ exhibiting slightly distorted trigonal bipyramidal coordination. First, by analogy with the conventional approach, we perform calculations by considering the $3d^8$ Ni ion electrons as being unconstrained to demonstrate the limitation of this analysis in reproducing the experimentally observed behavior. We then proceed with a thoroughgoing presentation of the mathematical approach, demonstrating the indispensable role of orbital constraints in unraveling the origin of all observations, emphasizing on all relevant settings and approximations. The effect on FSG resulting from the reduced electron degrees of freedom is analyzed in great detail. In particular, we show that the constrained electron dynamics is compulsory for the occurrence of large splitting in FSG and a non-negligible unquenched orbital angular momentum. A comparison between the theoretical and experimental results for the low-field susceptibility, magnetization, and EPR spectroscopy is discussed and displayed. In addition, the present research aims to provide insights for future investigations focused on molecular magnets consisting of metal centers with highly filled valence subshells. Furthermore, it aims to provide the basis for implying such constraints in alternative methods like the quantum perturbation ones, such as the second-order configuration active space perturbation theory (CASPT2) and *N*-electron valence state perturbation theory (NEVPT2), see ref 46 and references therein.

The rest of the paper is structured as follows. In Section II, we present a brief account on the applied method and introduce the mathematical notation for all observables and physical quantities used throughout the manuscript. Section III discusses the limitations of the conventional approach in calculating the energy spectrum of the studied complex and in reproducing its experimental magnetic behavior. In Section IV, we introduce the idea of constrained orbital dynamics and its potential to interpret the magnetic behavior of $3d^8$ complexes concentrating on the one that is under investigation here. This includes a thoroughgoing analysis of all ensuing approximations and settings. Section V is devoted to the comparison between the theoretical and experimental results of the studied complex. In Section VI, we discuss the effectiveness of the conventional single-ion spin Hamiltonian in the case of constrained orbital dynamics. Section VII summarizes the used method and obtained results.

II. THEORETICAL BACKGROUND

II.I. Generalities. To unravel the mechanisms underlying the magnetic properties of the compound $[\text{Ni}(\text{MDABCO})_2\text{Cl}_3]\text{ClO}_4$ ($\text{MDABCO}^+ = 1\text{-methyl-4-aza-1-azoniobicyclo}[2.2.2]\text{-octanium cation}$),³⁷ we make use of the method developed in ref 25. The named method considers the coordination complex as an effective spin-one system composed of Ni ion, eight electrons effectively localized around the Ni center, and five ligands regarded as effective point-like charges in the series expansion of CF potentials. In the resulting effective parameterization scheme, the effect of electron delocalization is accounted for by quantifying the charge negativity of a ligand with respect to the $3d$ electrons via a unique charge number. Furthermore, within the used parameterization scheme, one may account for constraints restricting the orbital dynamics of nonsinglet unpaired electrons. In general, all constraints are related to the emergence of phase differences in the electron direct exchange and field–orbital coupling. Here, we will restrict the study only to those constraints that do not break the invariance of the observables. A ball-and-stick representation of the distorted

trigonal bipyramidal structure of $[\text{Ni}(\text{MDABCO})_2\text{Cl}_3]^+$ in the first coordination sphere is shown in Figure 1.

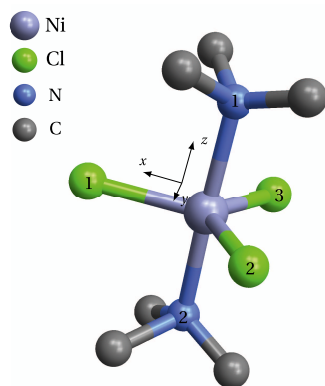


Figure 1. Ball-and-stick representation from the first coordination sphere of the complex $[\text{Ni}(\text{MDABCO})_2\text{Cl}_3]^+$. The structural parameters are provided by ref 37 and further given in spherical coordinates in Table 1 according to the depicted enumeration and reference frame. The z -axis is aligned along the principal one of an ideal trigonal coordination used as a benchmark.

Let us introduce some basic physical quantities used throughout the manuscript. By $\mu_n = (\mu_n^\alpha)_{\alpha \in \mathbb{K}}$, with $\mathbb{K} = \{x, y, z\}$, we denote the expectation value of the total magnetic moment operator associated with the n -th energy level with $|\mu_n| = \mu_n$. The corresponding spin and orbital angular momentum components are $\mu_{n,s}$ and $\mu_{n,b}$, respectively. As usual, κ denotes the orbital reduction coefficient, Z is the metal ion charge number, and Z_i is the i -th reactive nonmetal (ligand) charge number. A phase difference between two electrons occupying orbitals of types ν and τ is denoted by $\varphi_{\nu,\tau}$. In particular, the phase difference occurring in the process of direct exchange is represented as $\varphi_{\nu,\tau}^{\text{ex}}$. The energy barrier per single complex separating the spin-one fully polarized magnetic states is denoted by U_{eff} . The electric constant, magnetic constants, Bohr radius, and electron's g -factor are denoted as ϵ , μ_0 , r_B , and g_e , respectively. Furthermore, all energy levels are normalized, with a ground state taken equal to zero. The energy gap between i -th and j -th energy levels is denoted by E_{ij} . All magnetic moments are given in units of Bohr magneton μ_B . The z -axis is the quantization axis, and in the bracket notation, we use “1” to designate the spin state “-1”.

II.II. Hamiltonian. The Hamiltonian describing the magnetic properties of 3d⁸-based compounds (see e.g., Figure 1) reads

$$\hat{H} = \hat{U}_R(\mathbf{r}_1, \dots, \mathbf{r}_8) + \hat{U}_{\text{CF}}(\mathbf{r}_1, \dots, \mathbf{r}_8) + \hat{U}_{\text{SO}}(\mathbf{r}_1, \dots, \mathbf{r}_8) + \hat{U}_Z \quad (1)$$

where $\mathbf{r}_i = (r_i)_{\alpha \in \mathbb{K}}$ is the i -th electron position vector, and the operator corresponding to Coulomb interactions is given by

$$\hat{U}_R(\mathbf{r}_1, \dots, \mathbf{r}_8) = \frac{1}{2} \sum_{1 \leq i \neq j \leq 8} \frac{\gamma}{|\mathbf{r}_i - \mathbf{r}_j|}, \quad \gamma = \frac{e^2}{4\pi\epsilon}$$

The CF operator associated with the interactions between 3d electrons and the effective ligands with position vectors \mathbf{d} is expressed by

$$\hat{U}_{\text{CF}}(\mathbf{r}_1, \dots, \mathbf{r}_8) = \sum_k \sum_{1 \leq i \leq 8} \frac{\gamma Z_k}{|\mathbf{r}_i - \mathbf{d}_k|}$$

where k runs over the number of all ligands. The operator

$$\hat{U}_{\text{SO}}(\mathbf{r}_1, \dots, \mathbf{r}_8) = \frac{g_e \mu_0 \mu_B^2}{2\pi} \sum_{1 \leq i \leq 8} \frac{Z}{|\mathbf{r}_i|^3} \hat{\mathbf{l}}_i \cdot \hat{\mathbf{s}}_i \quad (2)$$

represents the spin–orbit interactions of relativistic origin and

$$\hat{U}_Z = -\mu_B \sum_{1 \leq i \leq 8} \mathbf{B} \cdot (\hat{\mathbf{l}}_i + g_s \hat{\mathbf{s}}_i)$$

takes into account the interaction of all 3d electrons with the externally applied magnetic field $\mathbf{B} = (B_\alpha)_{\alpha \in \mathbb{K}}$, with unit vector $\mathbf{n} = (n_\alpha)_{\alpha \in \mathbb{K}}$ and magnitude B . Here, $\hat{\mathbf{l}}_i$ and $\hat{\mathbf{s}}_i$ are the i -th electron's orbital and spin operators, respectively. The series expansion of Coulomb and CF potentials is discussed in ref 45. Note that the effect of all orbital and spin magnetic dipole–dipole interactions into FSG is found to be negligible and hence are omitted from eq 1. Moreover, all kinetic terms, electron–nuclei, and nuclei–nuclei ones are not given in eq 1, since on average their contribution is a constant that drops after the normalization.

III. CONSTRAINT FREE THEORY

Describing the magnetic properties of the complex $[\text{Ni}(\text{MDABCO})_2\text{Cl}_3]^{+37}$ only within the conventional analytic techniques and approximations^{11,25,38,47} turns out to be unfeasible as we have shown here. The energy spectrum of the compound obtained within these approaches is depicted in Figure 2 with the corresponding numerical representation given in the Supporting Material (Section S.5). The first energy gap shown in Figure 2b results from the distorted geometry and represents CF splitting between the configurations $d_{xz}^2 d_{yz}^2 d_{xy}^2 d_{x^2-y^2}^1 d_{z^2}^1$ and $d_{xz}^2 d_{yz}^2 d_{xy}^2 d_{x^2-y^2}^2 d_{z^2}^1$. Note that the orbital splitting diagram obtained only from CF calculations does not give the correct ground-state configuration. Here, it is displayed

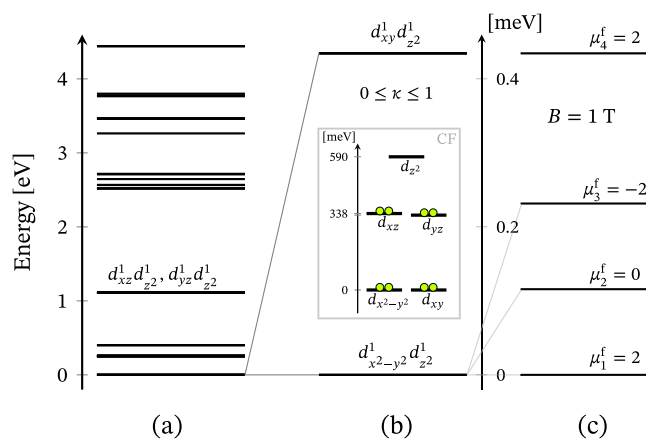


Figure 2. (a) Energy spectrum of the complex $[\text{Ni}(\text{MDABCO})_2\text{Cl}_3]^+$ in the absence of phase constraints. The calculations are performed with structural and intrinsic parameters given in Table 1. (b) First energy gap resulting from the action of CF, invariant with respect to the variations of κ . The inset depicts the orbital splitting and occupation obtained from the consideration of CF only. (c) Zeeman splitting for arbitrary orientation with respect to the complex's reference frame magnetic field. The superscript “f” indicates that, in this case, the quantization axis aligns along the field's direction.

for the sake of comparison to its counterparts obtained with the aid of other methods. Notice that the computed ground state configuration is the result of the dominant Coulomb interactions. In particular, the configurations $d_{xz}^1 d_{yz}^2 d_{xy}^2 d_{x^2-y^2}^2 d_z^1$ and $d_{xz}^2 d_{yz}^1 d_{xy}^2 d_{x^2-y^2}^2 d_z^1$ have a higher Coulomb correlation energy and therefore reside approximately 1.11 eV higher in the energy spectrum than the ground state one $d_{xz}^2 d_{yz}^2 d_{xy}^1 d_{x^2-y^2}^2 d_z^1$.

The absence of ZFS and hence the isotropic behavior evident from the Zeeman splitting depicted in Figure 2c is a consequence of the vanishing SO coupling between the obtained ground state $|\phi_{10,1,m}\rangle$ and first excited one $|\phi_{9,1,m}\rangle$, for all m . Details about the used state functions are given in the Supporting Material (Section S.1). SO interactions cannot generate a coupling in the case when the electrons are free from any constraints since the Pauli principle forbids the coupling between active and core orbitals. It is worth noting that in this case, the axial and rhombic ZFS parameters^{41–44} vanish. Thus, in the framework of the studied system, SO interactions between nonconstrained electrons exclude FS and thus cannot generate MA. Accordingly, the experimental findings of the magnetic properties of the complex $[\text{Ni}(\text{MDABCO})_2\text{Cl}_3]^+$ reported in ref 37 cannot be derived within the conventional approach.

In the quest for the origin of FSG and MA in the considered complex, we impose constraints on the 3d electron degrees of freedom and investigate their effect on the energy level sequence.

IV. OCCURRENCE OF CONSTRAINTS

IV.I. General Considerations. Relying only on the conventional approach that restricts the parameterization scheme to the action of CF and SO interactions can neither reduce the ground-state degeneracy nor invoke an additional coupling between the ground state and first excited states of the spectrum depicted in Figure 2b. We would like to point out that dipole–dipole magnetic interactions have a negligible contribution to FS and cannot be the origin of MA in the system under consideration. Therefore, we may rather assume that the ground-state magnetic properties can be strongly affected by the Coulomb interactions between nonsinglet paired electrons and the confinement of some degrees of freedom of these electrons. Such an assumption would necessarily require imposing additional constraints restricting the electron orbital motion while conserving all observables. The named constraints must obey the following prerequisites: (i) preserve the orthonormality of the initial basis states (see, e.g., the Supporting Material, Section S.1) ensuring energy invariance under the exchange symmetry and (ii) ensure the conservation of the square of total orbital angular momentum component of the unpaired electrons with respect to the quantization axis.

IV.II. Direct Exchange under a Phase Difference. The necessity of imposing constraints restricting the orbital dynamics of nonsinglet paired electrons involved in the direct exchange in complexes with highly filled valence subshells is tightly related to CF symmetry. Although the considered complex exhibits structural distortions, the d_z orbital always remains an active one. This limits the number of exchange integrals that will depend on the phase difference between the electrons occupying active orbitals to two. In terms of our notations (see the Supporting Material, Section S.2.1), the two exchange terms read

$$F_i = a_i \frac{\gamma Z}{r_B} [1 - \delta(\varphi_{\nu_i, z^2} - \varphi_{\nu_i, z^2}^{\text{ex}})] + f_i(\varphi_{\nu_i, z^2}, Z) \delta(\varphi_{\nu_i, z^2} - \varphi_{\nu_i, z^2}^{\text{ex}}), \quad i = 8, 9 \quad (3)$$

where $\nu_8 = xz$, $\nu_9 = xy$, $x^2 - y^2$, and $\delta(\cdot)$ is the Dirac delta function. The values of a_i and the explicit representation of the functions $f_i(\varphi_{\nu_i, z^2}, Z)$ are given in the Supporting Material (eqs S.4 and S.5), respectively. Accordingly, we end up with two pairs of 3d-orbital configurations with active electrons obeying the same constraint. For $\nu \neq \mu = xy, x^2 - y^2$, and $\alpha \neq \tau = xz, yz$, these are the configurations

$$d_{xz}^2 d_{yz}^2 d_{xy}^1 d_{x^2-y^2}^2 d_z^1 \quad \text{and} \quad d_{xz}^1 d_{yz}^2 d_{xy}^2 d_{x^2-y^2}^2 d_z^1 \quad (4)$$

with the corresponding states $|\phi_{9,1,m}\rangle$, $|\phi_{10,1,m}\rangle$, and $|\phi_{4,1,m}\rangle$, $|\phi_{7,1,m}\rangle$, respectively. In other words, the direct exchange involving the active orbitals $d_{x^2-y^2}^1 d_z^1$ and $d_{xy}^1 d_z^1$ will take place for $\varphi_{xy, z^2}^{\text{ex}} = \varphi_{x^2-y^2, z^2}^{\text{ex}}$. Similarly, for the remaining two pairs of active orbitals, $d_{xz}^1 d_z^1$ and $d_{yz}^1 d_z^1$, we have $\varphi_{xz, z^2}^{\text{ex}} = \varphi_{yz, z^2}^{\text{ex}}$. On the other hand, since the configurations eq 4 are separated by an energy gap of approximately $E_\Delta = 1.11$ eV (see Figure 2a), the following inequality always holds $\varphi_{\nu_8, z^2}^{\text{ex}} \neq \varphi_{\nu_9, z^2}^{\text{ex}}$. The values of these phases ensuring the invariance of the energy eigenvalues in the absence of SO interactions are of physical significance, where, for $i = 1, 2$, we have $\varphi_{\nu_i, z^2}^{\text{ex}} \in [-\pi, \pi]$.

IV.III. Phase Constraints to the Origin of FSG. According to the conventional study of coordination complexes, the electron orbital dynamics is calculated by considering the electron phases as independent variables over an infinite time. For complexes of highly filled subshells, such as the 3d⁸ ones, it means that an electron occupying an active orbital cannot couple to a core orbital neither under the influence of SO interactions nor under an externally applied magnetic field without violating the Pauli principle. As a result, the pairs of states $|\phi_{9,1,m}\rangle$, $|\phi_{10,1,m}\rangle$ and $|\phi_{4,1,m}\rangle$, $|\phi_{7,1,m}\rangle$ can neither be intracoupled under the action of CF nor by SO and Zeeman interactions obtaining $\langle d_{xy}, d_{xy} | d_{x^2-y^2}, d_{x^2-y^2} \rangle = 0$ and $\langle d_{xz}, d_{xz} | d_{yz}, d_{yz} \rangle = 0$, respectively.

The pertinent coupling, however, cannot be induced even by considering only a phase constraint occurring over the time of direct exchange between the electrons occupying active orbitals (see Section IV.II). The occurrence of such a coupling requires imposing two additional constraints that allow the electrons within each configuration given in eq 4 to be distinct by an orbital phase factor. This will ensure that these electrons cannot occupy the same state allowing for the occurrence of coupling between active and core orbitals without violating the exclusion principle.

In particular, for complexes of trigonal bipyramidal coordination, the dominant phase constraints are φ_{xy, x^2-y^2} and $\varphi_{xz, yz}$ that give rise to an overlap between the singlet states

$$\langle d_{xy}, d_{xy} | d'_{x^2-y^2}, d'_{x^2-y^2} \rangle = \cos(4\varphi_{xy, x^2-y^2}),$$

$$|\varphi_{xy, x^2-y^2}| \in (0, \frac{\pi}{8}] \quad (5a)$$

and

$$\langle d_{xz}, d_{xz} | d'_{yz}, d'_{yz} \rangle = \cos(2\varphi_{xz, yz}), \quad |\varphi_{xz, yz}| \in (0, \frac{\pi}{4}] \quad (5b)$$

without violating the orthonormality of the basis states given in the Supporting Material (Section S.1) and ensuring the energy invariance under the exchange symmetry. Here, the prime symbol indicates that there is a phase factor that couples the

Table 1. Intrinsic and Structural Parameters from the First Coordination Sphere of the Complex $[\text{Ni}(\text{MDABCO})_2\text{Cl}_3]^+$ with the Ball-and-Stick Representation Shown in Figure 1^a

cases	constituents	N ₁	N ₂	Cl ₁	Cl ₂	Cl ₃	Ni
	φ [deg]	0	0	0	117.03	236.76	
	ϑ [deg]	0	176.59	88.58	91.41	90.26	
	ϱ [Å]	2.191	2.196	2.310	2.318	2.315	
	Z	1.75	1.75	1.23	1.23	1.23	10
	$0 < \varphi_{xy,x^2-y^2} \leq \frac{\pi}{8}$						
c1	$\varphi_{\nu_9,z^2}^{\text{ex}} = 0.852656\pi$			$\varphi_{\nu_{8z^2}}^{\text{ex}} = 0.39155562\pi$; $\nu_9 = xy, x^2 - y^2$; $\nu_8 = xz, yz$			
	$0 < \varphi_{xz,yz} \leq \frac{\pi}{4}$						
c2	$\varphi_{\nu_9,z^2}^{\text{ex}} = 0.764588252\pi$			$\varphi_{\nu_{8z^2}}^{\text{ex}} = 0.27448137\pi$; $\nu_9 = xy, x^2 - y^2$; $\nu_8 = xz, yz$			

^aWe have the radial distance ϱ , azimuthal angle φ , and the polar one ϑ for each reactive nonmetal surrounding the nickel ion. The effective charge numbers of all ions obtained from the comparison with the experimental data from ref 37 are given in the 5-th row. The 7-th and 9-th rows present the values of the phase differences resulting within the processes of direct exchange between the electrons occupying active orbitals. The allowed range of the phases φ_{xy,x^2-y^2} and $\varphi_{xz,yz}$ is specified in the 6-th and 8-th row, respectively.

named orbitals. For more details, the reader may consult Section S.3 in the Supporting Material.

As a consequence of eq 5, we end up with additional SO terms, see, e.g., the Supporting Material (eq S.6). Furthermore, we have an additional coupling of the electrons orbital angular momentum to the externally applied magnetic field (see the Supporting Material, eq S.7). These terms describe the interaction of unquenched orbital angular momenta (see the Supporting Material, Section S.2.5) with the externally applied magnetic field. Note that eq 5 does not hold for singlet excited states consisting completely of core orbitals. Therefore, unlike 3d² systems, the coupling phases (eq 5) make the origin of FSG and associated orbital unquenching in 3d⁸ trigonal bipyramidal complexes unique. In this respect, it is essential to point out that the probability to observe intercoupling between the groups $|\phi_{9,1,m}\rangle$, $|\phi_{10,1,m}\rangle$ and $|\phi_{4,1,m}\rangle$, $|\phi_{7,1,m}\rangle$ equals zero.

IV.IV. Microscopic States. The occurrence of coupling phases described in Sections IV.II and IV.III stands as a fundamental feature of 3d⁸ complexes in the considered symmetry. However, since we consider the system as isolated, the phases in eq 5 will not change in time, unless we expose the system to an external influence. This suggests that in the presence of only SO interactions, the phase differences φ_{xy,x^2-y^2} and $\varphi_{xz,yz}$ will take values corresponding to a small or negligible orbital overlap. Thus, SO interactions cannot give rise to phase differences with values approaching the zero boundary. This may be achieved by applying a dc external magnetic field or equivalently an electromagnetic one.

Within all considered approximations, the present method predicts the existence of two energetically equally favorable microscopic states, namely, **c1** and **c2**, related to the two pairs of configurations given in eq 4, respectively. For the considered complex, we obtain the unique set of values corresponding to **c1** and **c2** (see Table 1). We would like to point out that the phase values $\varphi_{\nu_9,z^2}^{\text{ex}} = 0.852656\pi$ and $\varphi_{\nu_{8z^2}}^{\text{ex}} = 0.27448137\pi$ are related to the conservation of the ground state energy in the absence of SO interactions. For clarity, the corresponding energy minima are depicted in Figure 3. The remaining ones, $\varphi_{\nu_9,z^2}^{\text{ex}} = 0.764588252\pi$ and $\varphi_{\nu_{8z^2}}^{\text{ex}} = 0.39155562\pi$, ensure that the energy gap E_{Δ} remains invariant. Note that, since all other exchange integrals do not depend on these phases, the eigen energies are conserved. The phase differences φ_{xy,x^2-y^2} and $\varphi_{xz,yz}$ defining the overlap integrals eqs 5a and 5b, respectively, can take values within the given range only in the presence of an externally applied

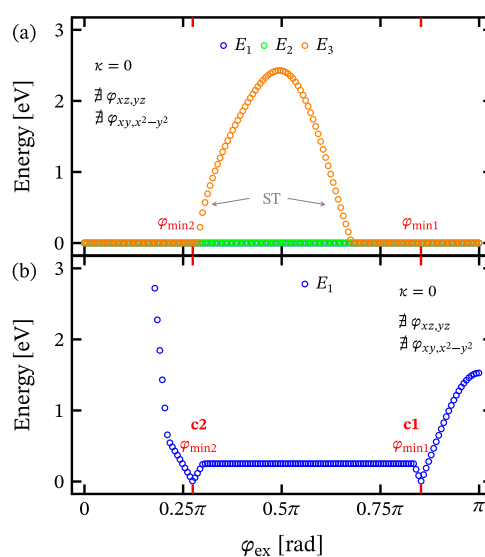


Figure 3. (a) Dependence of the first three energy levels on the phase difference occurring in the process of direct exchange between electrons occupying the active orbitals in eq 4 and in the absence of SO and Zeeman interactions. All energy levels are normalized to the ground state one E_1 . The abbreviation “ST” stands for singlet–triplet transitions and marks the domain of singlet ground states. The orange circles correspond to a superposition of triplet states and zero net magnetic moment. (b) Depicts only the dependence of the ground state energy prior to normalization. Once SO and Zeeman interactions are taken into account, we observe the occurrence of coupling phases $\varphi_{xz,yz}$ and φ_{xy,x^2-y^2} (see eq 5) giving rise to FSG at the given minima. In both subfigures, $\varphi_{\text{min1}} = 0.27448137\pi$ and $\varphi_{\text{min2}} = 0.852656\pi$, see Table 1.

magnetic field or any other source that can generate an additional phase factor.

The two microscopic states, **c1** and **c2**, conform to FSG shown in the Supporting Material (Figures S.1b and S.2b). The values of B and κ shown in the latter figures are selected for the explanatory purpose and sake of comparison and are not related to the experimental data discussed in the forthcoming sections. Each of the obtained states is distinct by FS and the extent of orbital unquenching. As shown in Figures S.3b and S.4b in the Supporting Material, for the same value of κ , **c1** is characterized by the largest energy gaps. In this case, a huge splitting shows up. Nevertheless, the obtained FSG is not a signature of huge ZFS since it is triggered and governed by the externally applied magnetic field. Although the phases in eqs 5a and 5b vanish at

very large magnetic fields, the cases depicted in Figures S.3b and S.4b in the Supporting Material elucidate the extent of FSG in the studied system.

The state **c1** corresponds to a higher extent of orbital unquenching. For example, at $B = 2$ T, $n_x = n_y = n_z = \frac{1}{\sqrt{3}}$, $\kappa = 1$, and $\varphi_{xy, x^2-y^2} = 0.0833333\pi$, we obtain the ground-state magnetic moment $\boldsymbol{\mu}_1 = (0, 0, 1)$ with orbital and spin components, respectively, $\boldsymbol{\mu}_{1,l} = (0, 0, -0.999871)$ and $\boldsymbol{\mu}_{1,s} = (0, 0, 1.99989)$. Under the same orientation and magnitude of the magnetic field, the value of orbital reduction factor and $\varphi_{xz,yz} = 0.166666\pi$, in the state **c2**, we get $\boldsymbol{\mu}_1 = (0.0439067, 0, 0.18699)$, $\boldsymbol{\mu}_{1,l} = (0, 0, -0.0577732)$, and $\boldsymbol{\mu}_{1,s} = (0.0439067, 0, 0.244763)$. For more details, see, e.g., the Supporting Material (Figure S.5) showing the ground-state magnetic moment dependence on κ at the boundary values of phase differences φ_{xy, x^2-y^2} .

V. MAGNETIC PROPERTIES

V.I. Theoretical Relations and Parameters. The experimental measurements of the magnetic properties of $[\text{Ni}(\text{MDABCO})_2\text{Cl}_3]^+$ based on powder and single crystal samples are reported in ref 37. Here, we study the low-field magnetic susceptibility, magnetization, and EPR spectra shown in Figures 5 and 6, respectively. An analysis within the framework of the theoretical approach developed above taking into account the experimental data reveals unequivocally that **c2** is the only possible state. In **c1**, the low-field EPR and susceptibility measurements cannot be reproduced. The successful fitting to the experimental data yields the charge number values given in the 5-th row in Table 1. Furthermore, it gives the minimal value $\kappa = 0.16$ related to the d_z orbital and $\kappa = 1$ for the remaining ones.

The energy spectrum of the studied complex with three main FSG cases is depicted in Figure 4a. Note that the shown spin-one states are included for the purpose of clarity and do not conform to the total magnetic moments (see, e.g., the Supporting Material, Section S.6).

The first case shown in Figure 4b describes the obtained CF splitting and a very small ZFS, with $\varphi_{xz,yz} = 0.248\pi$. Represented as an effective spin-one state functions, the first three eigenstates read

$$|\Psi_1\rangle \equiv \frac{1}{\sqrt{2}}(|1\rangle + |\bar{1}\rangle), \quad |\Psi_2\rangle \equiv \frac{1}{\sqrt{2}}(|1\rangle - |\bar{1}\rangle), \quad |\Psi_3\rangle \equiv |0\rangle.$$

The second case depicted in Figure 4c corresponds to the saturation of the magnetization, with $\varphi_{xz,yz}^{(s)} = 0.185\pi$ and $B_s \approx 4.2$ T. Here, for $B = B_z \geq 4.2$ T, the value of the coupling phase remains constant, indicating the maximal rate of orbital unquenching. When the field has transverse components, $\varphi_{xz,yz}$ is no longer constrained and can decrease further approaching zero. In the interval $\varphi_{xz,yz} \in (0, 0.185\pi]$, we derive the exact analytical expression (see the Supporting Material, Section S.4),

$$\varphi_{xz,yz} = \frac{1}{2} \arccos \left[\left(1 + \frac{B_m}{B_s} \right) \frac{\cos(2\varphi_{xz,yz}^{(s)})}{1 + \frac{B_m}{B_s} |\cos(\theta)|} \right]$$

where $\theta = (\widehat{\mathbf{Bz}})$, with $0 \leq \theta \leq \pi$, is the field's radial angle and B_m is the minimal value of $\mathbf{B} \perp z$ in the limit $\varphi_{xz,yz} \rightarrow 0$. FSG at $\theta = 0.49315581\pi$ and $B = 30$ T is shown in Figure 4d.

V.II. Susceptibility and Magnetization. A comparison between the theoretical and experimental data for the low-field

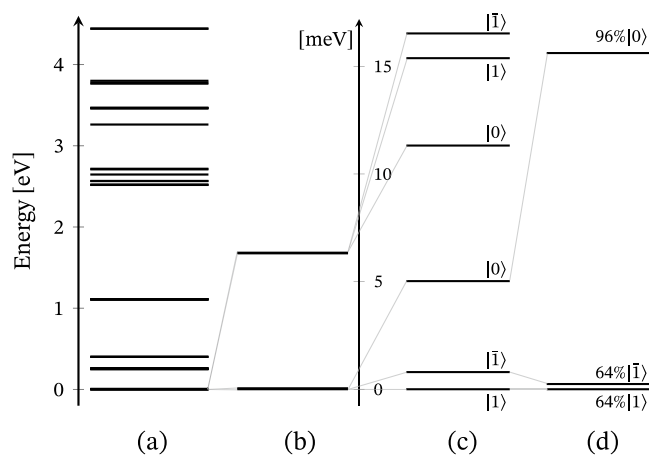


Figure 4. (a) Zero-field energy spectrum of the complex $[\text{Ni}(\text{MDABCO})_2\text{Cl}_3]^+$. The calculations are carried out taking into account the phase constraints, with the relevant structural and intrinsic parameters given in Table 1 and Section V.I. The corresponding numerical representation is given in the Supporting Material (Section S.5). (b) Depicts CF splitting and the small ZFS (first bold line) obtained for $\varphi_{xz,yz} = 0.248\pi$. (c) Displays the case with $B = B_z = 4.2$ T and $\varphi_{xz,yz} = 0.185\pi$ obtained at the saturation of the magnetization. (d) Depicts FSG at $B = 30$ T and $\varphi_{xz,yz} \rightarrow 0$, with the magnetic field oriented very closely to the (x, y) plane of the studied complex. For clarity, only the highest probability spin-one triplets are depicted. The complete representations of the corresponding eigenstates are given at the end of Section V.III.

magnetic susceptibility as a function of the temperature is shown in Figure 5, where the ratio between molar mass and density

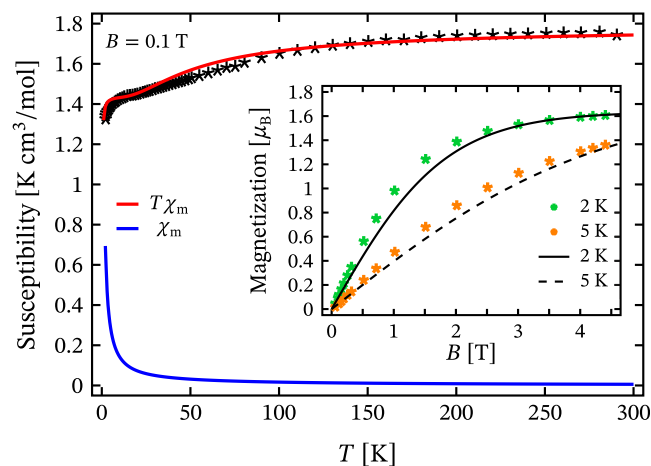


Figure 5. Temperature dependence of low-field magnetic susceptibility χ_m of the studied complex. The magnetization as a function of an externally applied magnetic field is depicted in the inset, where the five pointed star symbols represent the experimental data from ref 37. The solid and dashed lines present the theoretical results obtained using the parameter values given in Table 1 and discussed in Section V.II.

equals unity. In the given temperature range and magnetic field value, the average of the corresponding coupling phase is estimated to be $\varphi_{xz,yz} = 0.2475\pi$, within the interval $0.2465\pi < \varphi_{xz,yz} < 0.2485\pi$. This result suggests that SO interactions alone generate a phase difference of approximately $\varphi_{xz,yz} \approx 0.2485\pi$ or slightly larger. With the aid of EPR data, on the other hand, we adjust this value to 0.248π . The value of ZFS is very small with the first and second excited energy levels almost overlapping.

Accordingly, at $B = 0.1$ T, we have two very closely lying excited states. The associated energy gaps are $E_{21} \approx 0.032$ meV and $E_{31} \approx 0.059$ meV. These results shed light on the appearance of the small plateau in the range $5 < T < 17$ K in the $T\chi_m$ curve in Figure 5. The population rates of the corresponding excited energy levels increase rapidly in the temperature range $0 < T \leq 5$ K, and at $T \rightarrow 17$ K, both are equally occupied. In particular, at $T = 17$ K, we have $p_1 \approx 33.5\%$, $p_2 \approx 32.8\%$, and $p_3 \approx 32.2\%$, where for $i = 1, 2, 3$, p_i are the corresponding population rates. However, we have three additional excited energy levels (see Figure 4b) that above $T = 17$ K slowly get populated giving rise to a small magnetization moment. The population of these levels then gradually increases reaching its maximum $p_i \approx 14.3\%$ at $T = 250$ K, where $i = 4, 5, 6$, thus giving rise to a broad demagnetization step in the range $17 < T \leq 250$ K that is more clearly visible in the case $T\chi_m$ depicted by red circles in the Supporting Material (Figure S.6).

The magnetization depicted in the inset of Figure 5 confirms the analysis of the susceptibility data. Further results are shown in the Supporting Material, Figure S.7. Statistically speaking, at 2 K and for small magnetic fields, the three components of the complex's magnetic moment contribute with almost equal probability weights. The increase in the magnetic field's magnitude, however, favors only the z component. For example, at $B = 0.1$ T and $T = 2$ K, the x , y , and z components of the calculated magnetization read 0.0905293, 0.0829337, and 0.0938138 Bohr magnetons, where $\varphi_{xz,yz} = 0.2475\pi$. Note that for the evaluation of each component, the magnetic field was aligned along the respective axis. On the other hand, at $B = 4.6$ T and the same temperature value, for the respective components, we get 0.215797, 0.186354, and 1.61527, where $\varphi_{xz,yz} = 0.185\pi$. These results indicate that the observed axial MA is governed by the coupling phase values. Accordingly, for $B < 1$ T, we observe a prompt increase of magnetization. As the magnetic field increases by magnitude, the orbital coupling surges, leading to a higher extent of orbital unquenching and hence a smaller total magnetic moment calculated per single nickel center. Subsequently, the magnetization reaches saturation values below the expected $2 \mu_B$.

At weak magnetic fields, the first excited state lies very close to the ground state. Therefore, the population promptly increases with the temperature and at 5 K, we observe an almost linear dependence of the magnetization as a function of B . As a result, at the given temperature, the saturation level is reached by approaching the value $B = 7$ T, see the Supporting Material (Figure S.7).

V.III. EPR Spectra. In addition to the study of the low-field susceptibility and the magnetization, we analyze the field dependence of the experimental EPR intensity peaks reported in ref 37 depicted in Figure 6. A striking feature of the low-field powder spectrum is the prompt increase of the absorption frequency as the magnitude of B increases. The energy difference between intensity peaks at 0.5 and 2 T is about 0.6 meV (150 GHz), which is highly above the energy value that can be generated only by the Zeeman interactions in the presence of strong SO coupling and hence large ZFS. Such a strong field dependence of low-field EPR peaks indicates that ZFS is only seemingly huge and that there is an addition to the linear field dependence provided by spin Zeeman interactions. As discussed in Section IV.III and demonstrated in Section V.II, the occurrence of the coupling phase $\varphi_{xz,yz}$ reflects such an effect. It generates an orbital angular momentum that alters the linear dependence of FS on the externally applied magnetic field.

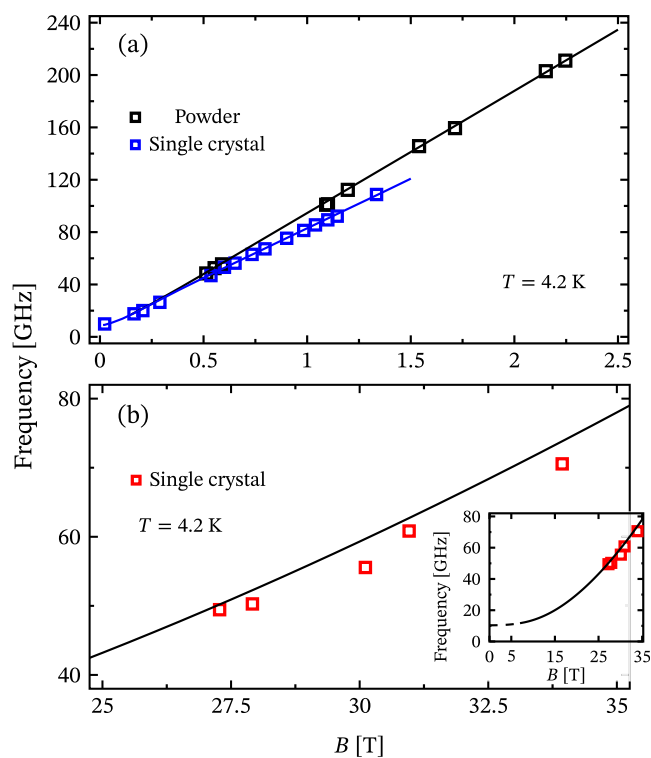


Figure 6. Frequency vs external magnetic field plot of EPR peaks for powder and single crystal samples with experimental data (squares) from ref 37. The theoretical results are presented by solid lines. The calculations are carried out with the parameter values given in Table 1. (a) Depicts the low-field EPR peaks with single crystal measurements carried out at approximately $\frac{\pi}{6}$ from the axis associated with the highest intensity peak based on the powder data. (b) High-field EPR results, with the magnetic field oriented within the (xy) plane of the studied compound. The dashed line corresponds to the field domain $0 \leq B \leq 6.37539$ T, with $0.248\pi \geq \varphi_{xz,yz} \geq 0$.

We would like to point out that hereafter, we use the selection rules $|\Delta m| = 1, 2$ after refs 42, 48. The frequency-field dependence of the powder peaks depicted in Figure 6a is well described for magnetic field directions forming angles ranging between $\frac{\pi}{3}$ and $\frac{\pi}{6}$ from the z -axis. The highest probability for resonance is reached at $\frac{\pi}{3}$ or $n_x = n_y = \pm\sqrt{\frac{3}{8}}$ and $n_z = \pm\frac{1}{2}$. All transitions correspond to $\Delta m = \pm 1$ and within the range $0.5 \text{ T} \leq B \leq 2.5 \text{ T}$, and we observe a decrease in the phase difference, $0.2415\pi \geq \varphi_{xz,yz} \geq 0.2295\pi$. As an example, at 0.5 T, we get the energy gaps $E_{21} \approx 0.06$ meV and $E_{31} \approx 0.22$ meV, with eigenstates' probability coefficients presented in percentage $|\Psi_1\rangle \rightarrow \{89.2\%|1\rangle, 6.92\%|\bar{1}\rangle, 3.88\%|0\rangle\}$, $|\Psi_2\rangle \rightarrow \{8.63\%|1\rangle, 87.4\%|\bar{1}\rangle, 3.97\%|0\rangle\}$, and $|\Psi_3\rangle \rightarrow \{2.56\%|1\rangle, 4.63\%|\bar{1}\rangle, 92.8\%|0\rangle\}$. Since at 4.2 K, the ground state and first excited one are almost equally populated, we have two energetically very close excitations associated with the two spin states of the incident microwave photons, thus giving rise to the observed peak at around 0.21 meV. By increasing the magnetic field magnitude, $\varphi_{xz,yz}$ drops to approximately 0.2295π , yielding a larger second ground-state energy gap. In particular, at $B = 2.25$ T, we have $E_{31} \approx 0.86$ meV. The probability coefficient in the corresponding eigenstates remains almost unchanged.

Within our approach, the low-field single crystal peaks (see Figure 6a) correspond to the cases when the magnetic field

direction forms angles within the interval $(0, \frac{\pi}{6})$ with respect to z -axis. The same peaks are visible in the simulations of powder data and hence correspond to $\Delta m = \pm 1$ transitions. However, for larger values of B , their intensity is approximately two times smaller. For comparison with the powder peak at $B = 0.5$ T and $\varphi_{xz,yz} = 0.2415\pi$, when the field is aligned along the z -axis, we obtain an energy transition of the same value, i.e., approximately 0.21 meV, but with eigenstates $|\Psi_1\rangle \rightarrow 99\%|1\rangle, |\Psi_2\rangle \rightarrow 99\%|\bar{1}\rangle$, and $|\Psi_3\rangle \equiv |0\rangle$. For $B \leq 0.15$ T, we get $\varphi_{xz,yz} = 0.248\pi$. Interestingly, since for $B \leq 0.1$ T, the gap between the first and the second excited energy levels is very small, and the corresponding EPR peaks may be misinterpreted as a transition with $\Delta m = \pm 2$. For the studied complex, the latter is forbidden when B is aligned along the easy axis and hence very unlikely to be observed. Nevertheless, when the magnetic field is strong enough and oriented at a small angle relative to the (x, y) plane of the studied complex, the energy eigenstates are represented as a proper mixture of all three spin-one states, thus increasing the probability to detect the effectively designated $\Delta m = \pm 2$ transitions.

The frequency-field dependence of high-field EPR transition shown in Figure 6b is reproduced for magnetic field unit vector components $n_\alpha = \pm 0.70695$ and $n_z = \pm 0.0215$ and phase difference $\varphi_{xz,yz} \rightarrow 0$ for $B \geq 6.37539$ T, where $\alpha = x, y$. In the range $0 \leq n_\alpha \leq 0.999769$, we observe a negligible variation in the results. The energy gap associated with the spin-one state $|0\rangle$ is very large (see Figure 4d), and hence, the peaks correspond only to the first ground-state magnetic excitation. For example, at $B = 30$ T, we have $E_{21} \approx 0.24$ meV and $E_{31} \approx 15.6$ meV, with energy eigenstates $|\Psi_1\rangle \rightarrow \{64\%|1\rangle, 33\%|\bar{1}\rangle, 3\%|0\rangle\}$, $|\Psi_2\rangle \rightarrow \{35\%|1\rangle, 64\%|\bar{1}\rangle, 1\%|0\rangle\}$, and $|\Psi_3\rangle \rightarrow \{2\%|1\rangle, 2\%|\bar{1}\rangle, 96\%|0\rangle\}$. We would like to point out that high-field EPR transitions are very sensitive to variations in the magnetic field direction with respect to z -axis, thus rendering the extraction of the data a tedious task. For example, if at $B = 30$ T, we change $|n_z|$ from 0.0215 up to 0.1, equal to an angle difference of about $\frac{\pi}{40}$, then the corresponding peak completely vanishes.

VI. OUTLOOK TO THE EFFECTIVE SINGLE-ION SPIN HAMILTONIANS

An essential consequence of the theoretical analysis introduced in Section IV is that the corresponding parameterization scheme of a generalized perturbation approach for studying complexes of highly filled valence subshells must necessarily account for the occurrence of coupling phases beforehand. However, gaining knowledge of the explicit expressions of all relevant parameters as a function of such phases requires a rigorous mathematical derivation that lies beyond the scope of the present research. Such a theoretical framework merits a separate study to be presented elsewhere and we believe it would be of great benefit to a broader scientific community.

A representative case is the origin of FSG in the studied complex showing the dependence on the phase difference $\varphi_{xz,yz}$ of the eigenvalues of the most considered effective single-ion spin Hamiltonians, namely

$$\hat{H}_D = \hat{s} \cdot \mathcal{D} \cdot \hat{s} \quad \text{and} \quad \hat{H} = \frac{D}{3} (3\hat{s}_z^2 - s(s+1)) + E(\hat{s}_x^2 - \hat{s}_y^2) \quad (6)$$

where for $\alpha = x, y, z$, $\hat{s} = (\hat{s}_\alpha)$ represents the effective spin-one operator, D and E denote the axial and rhombic FSG parameters, respectively, and \mathcal{D} is a traceless symmetric tensor with real elements. Note that in this case, the parameters in eq 6 are no

longer related to the conventional ZFS, except when $\varphi_{xz,yz} \geq 0.248\pi$, see the Supporting Material, Section S.4. We would like to stress, furthermore, that the corresponding effective g-factor will also depend on the coupling phase. For more details about the conventional relations between the parameters in eq 6, the reader may consult refs 41, 42, 44.

After Section V, we have $D = D(\varphi_{xz,yz})$ and $E = E(\varphi_{xz,yz})$. To find the maximal value of the axial parameter, we have to take the lower limit of the phase $\varphi_{xz,yz}$ corresponding to the high-field EPR line shown in Figure 6b and in particular to FSG depicted in Figure 4d. Thus, in the limit $\varphi_{xz,yz} \rightarrow 0$, we obtain $D \approx -121$ cm⁻¹ and $E \approx 0.38$ cm⁻¹. In the absence of phase constraints, these parameters vanish, see the discussion in Section III.

VII. RESULTS AND DISCUSSION

In the quest to elucidate the microscopic mechanisms that govern the magnetic behavior specific to the class of 3d⁸ mono- and polynuclear nanomagnets, we devise a method to diagonalize the corresponding generic Hamiltonian and compute the relevant fine structure of the total energy spectra. The obtained theoretical results are compared to their experimental counterparts for the spin-one single-ion magnet [Ni(MDABCO)₂Cl₃]ClO₄. The diagonalization procedure (see Section II.1) is based on the multiconfigurational self-consistent field method. In addition to the conventional mathematical framework that considers the electron orbital phases as independent variables over an infinite time, the present method necessarily accounts for quantum mechanical constraints that confine the 3d electron orbital motion under the conservation of all associated to the initial basis states observables.

The named constraints follow naturally from the thorough analysis of the electron correlations in 3d⁸ trigonal bi- and pyramidal coordination complexes. The results of this analysis unequivocally point out to a vanishing FSG in the case when the electron orbital dynamics is not constrained. This is a consequence of the Pauli principle that disallows a coupling between the active and core orbitals from the 3d configurations given in eq 4. Yet, FSG shows up due to the occurrence of orbital phase differences (see Section IV.III) that increase the probability for active to core orbital coupling via SO and Zeeman interactions without violating the exclusion principle.

Principally, by studying the magnetic behavior of the spin-one mononuclear nanomagnet [Ni(MDABCO)₂Cl₃]ClO₄, we found no evidence of huge ZFS or giant MA originating from SO interactions alone. Yet, we obtain SO-driven nontrivial FSG with a large overall splitting only in the case when the electron orbital dynamics obey constraints depending upon the interaction of the system with its surrounding medium. The electrons are found to be delocalized, with ligands showing larger negativity ($Z_N = 1.75$) along the nitrogen bonds and reduced Ni effective positive charge, see Table 1. In particular, we obtain very good agreement with the experimental observations (see Section V) pointing to the appearance of a very small ZFS depicted in Figure 4b and modest intrinsic MA energy at the zero- and low-field limits and in the absence of interactions with external sources. The corresponding magnetization reversal barrier showing the rate of the inherent magnetic anisotropy is depicted in Figure 7. The obtained energy barrier's height of about 27 K and relaxation time $\tau \approx 17$ μ s are in good agreement with the ranges (25–28 K) and (16–17 μ s), respectively, obtained from the ac susceptibility measurements reported in ref 37.

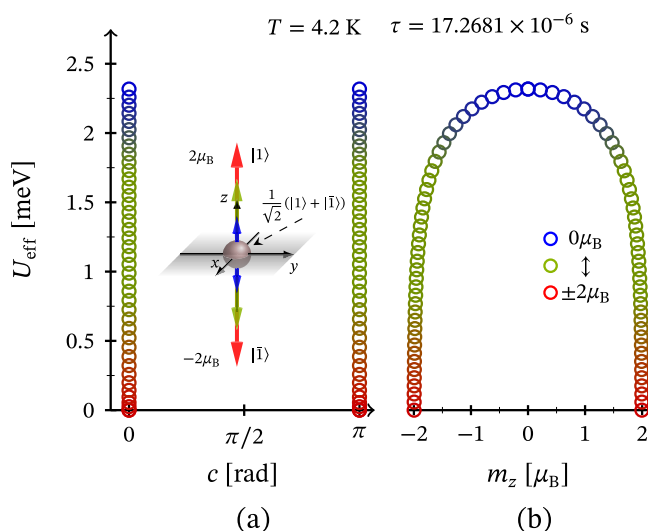


Figure 7. Energy barrier of the studied complex obtained at the zero-field limit depicted in Figure 4b, with $\varphi_{xz,yz} \rightarrow 0.248\pi$. The temperature is selected to match that from the EPR measurements providing the zero-field limit of $\varphi_{xz,yz}$. The given relaxation time τ is obtained using the Arrhenius equation for attempt time $\tau_0 = 2.86 \times 10^{-8}$ s. The barrier's height is about 2.3175 meV or 26.8 K. (a) Shows the barrier as a function of the direction angle c taken between the principle axis from the used as a benchmark ideal trigonal bipyramidal CF and the complex's total magnetic moment expectation value. (b) Depicts the corresponding barrier's profile calculated with respect to z component of the complex's total magnetic moment expectation value at the given temperature.

When the system is exposed to an external influence, however, as a result of the phase constraints (see Section IV), the energy gaps in FSG and MA change rapidly. We obtain a strong dependence of the relevant FSG on the externally applied magnetic field related to a significant splitting and orbital unquenching that rises with the occurrence of the phase constraint eq 5b. In contrast to the calculated upper bound of axial parameter $D \approx 535 \text{ cm}^{-1}$ reported in ref 37, we get large, but not huge splitting (120 cm^{-1}), that is underpinned by the occurrence of coupling phase $\varphi_{xz,yz}$. For comparison, almost identical values ($D \leq -120 \text{ cm}^{-1}$ and $E \approx 1.6 \text{ cm}^{-1}$) are reported by ref 35 in studying the magnetic behavior of the species $[\text{Ni}(\text{Me}_6\text{tren})\text{Cl}]\text{ClO}_4$, exhibiting similar distortion. These results are further confirmed by the far infrared measurements,³⁹ with the corresponding transition centered approximately at 111 cm^{-1} . Nevertheless, the origin of such nontrivial ZFS was not elucidated and neither the genuine contribution of SO interactions nor the effect of phase constraints were studied so far. As a result, different suggestions for the emergence of huge ZFS ($200 \leq |D| \leq 600 \text{ cm}^{-1}$) elusively gain ground. Therefore, we would like to emphasize that according to the present study in the absence of phase constraints, the axial and rhombic parameters vanish, see the discussion in Section III. Moreover, the corresponding coupling phase depends strongly on the application of external influence, in particular on the action of an applied external magnetic field (see Section V) leading to energy gaps in FSG larger than those resulting from the Zeeman interactions alone, making the overall splitting in FSG seemingly huge from the perspective of the conventional approach. The same dependence renders the intrinsic axial MA seemingly giant and the unquenched orbital angular momentum as a non-vanishing feature of the system.

In conclusion, the occurrence of phase differences as described in Section IV appears as a fundamental quantum feature of $3d^8$ nanomagnets with local trigonal bi- and pyramidal coordination. In general, the probability for observing constrained electron dynamics in coordination complexes with highly filled 3d subshells differ from zero and their occurrence does not depend on the extent of electron delocalization. Therefore, once included in the parameterization scheme of alternative quantum mechanical methods, the introduced relations and approximations may play an essential role in future theoretical investigations. As an example, the occurrence of coupling phases can be further taken into account in the quantum perturbation methods like CASPT2 and NVEPT2 ones, justifying the applicability of effective single-ion spin Hamiltonians, see the brief discussion in Section VI.

■ ASSOCIATED CONTENT

Supporting Information

The Supporting Information is available free of charge at <https://pubs.acs.org/doi/10.1021/acsomega.3c03208>.

Representation of initial basis states and single electron ones; matrix elements of the Coulomb, crystal field, spin-orbit, and Zeeman interactions; unquenched orbital momentum and overlaps; coupling phase; numerical representation of different energy spectra and related magnetic moments' expectation values; representation of energy eigenstates; figures of discussed energy spectra, low-field magnetic susceptibility, and magnetization (PDF)

■ AUTHOR INFORMATION

Corresponding Authors

Miroslav Georgiev – Bulgarian Academy of Sciences, G Nadjakov Institute of Solid State Physics, 1784 Sofia, Bulgaria; orcid.org/0000-0003-0598-3360; Email: mgeorgiev@issp.bas.bg

Hassan Chamati – Bulgarian Academy of Sciences, G Nadjakov Institute of Solid State Physics, 1784 Sofia, Bulgaria; orcid.org/0000-0002-0831-6945; Email: chamati@issp.bas.bg

Complete contact information is available at: <https://pubs.acs.org/doi/10.1021/acsomega.3c03208>

Notes

The authors declare no competing financial interest.

■ ACKNOWLEDGMENTS

This work was supported by the Bulgarian National Science Fund under grant no. KII-06-H38/6 and the National Program “Young scientists and postdoctoral researchers-2” approved by DCM 206/07.04.2022.

■ REFERENCES

- Gatteschi, D.; Sessoli, R.; Villain, J. *Molecular Nanomagnets*; Oxford University Press: New York, 2006.
- Winpenny, R. *Molecular Cluster Magnets*, World Scientific Series in Nanoscience and Nanotechnology; World Scientific, 2011; Vol. 3.
- Molecular Nanomagnets and Related Phenomena; Structure and Bonding*; Gao, S., Ed.; Springer: Berlin, 2015; Vol. 164.
- Sessoli, R. Magnetic molecules back in the race. *Nature* **2017**, *548*, 400–401.

- (5) Coronado, E. Molecular magnetism: from chemical design to spin control in molecules, materials and devices. *Nat. Rev. Mater.* **2020**, *5*, 87–104.
- (6) Giansiracusa, M. J.; Gransbury, G. K.; Chilton, N. F.; Mills, D. P. Single-Molecule Magnets. In *Encyclopedia of Inorganic and Bioinorganic Chemistry*, 1st ed.; Scott, R. A., Ed.; Wiley, 2021; pp 1–21.
- (7) Wang, J.-H.; Li, Z.-Y.; Yamashita, M.; Bu, X.-H. Recent progress on cyano-bridged transition-metal-based single-molecule magnets and single-chain magnets. *Coord. Chem. Rev.* **2021**, *428*, No. 213617.
- (8) Zhuo, Z.; Li, G.; Huang, Y. Understanding Magneto Structural Correlations Toward Design of Molecular Magnets. In *Advanced Structural Chemistry*; Cao, R., Ed.; Wiley, 2021; pp 777–832.
- (9) Atanasov, M.; Aravena, D.; Suturina, E.; Bill, E.; Maganas, D.; Neese, F. First principles approach to the electronic structure, magnetic anisotropy and spin relaxation in mononuclear 3d-transition metal single molecule magnets. *Coord. Chem. Rev.* **2015**, *289–290*, 177–214.
- (10) Feng, M.; Tong, M.-L. Single Ion Magnets from 3d to 5f: Developments and Strategies. *Chem. Eur. J.* **2018**, *24*, 7574–7594.
- (11) Georgiev, M.; Chamati, H. Single-Ion Magnets with Giant Magnetic Anisotropy and Zero-Field Splitting. *ACS Omega* **2022**, *7*, 42664–42673.
- (12) Schnack, J.; Brüger, M.; Luban, M.; Kögerler, P.; Morosan, E.; Fuchs, R.; Modler, R.; Nohjiri, H.; Rai, R. C.; Cao, J.; Musfeldt, J. L.; Wei, X. Observation of field-dependent magnetic parameters in the magnetic molecule $\{\text{Ni}_4\text{Mo}_{12}\}$. *Phys. Rev. B* **2006**, *73*, No. 094401.
- (13) Kostyuchenko, V. V. Non-Heisenberg exchange interactions in the molecular magnet $\text{Ni}_4\text{Mo}_{12}$. *Phys. Rev. B* **2007**, *76*, No. 212404.
- (14) Nehr Korn, J.; Höck, M.; Brüger, M.; Mutka, H.; Schnack, J.; Waldmann, O. Inelastic neutron scattering study and Hubbard model description of the antiferromagnetic tetrahedral molecule $\text{Ni}_4\text{Mo}_{12}$. *Eur. Phys. J. B* **2010**, *73*, 515–526.
- (15) Furrer, A.; Krämer, K. W.; Strässle, T.; Biner, D.; Hauser, J.; Güdel, H. U. Magnetic and neutron spectroscopic properties of the tetrameric nickel compound $[\text{Mo}_{12}\text{O}_{28}(\mu_2\text{-OH})_9(\mu_2\text{-OH})_3\{\text{Ni}(\text{H}_2\text{O})_3\}_4] \cdot 13\text{H}_2\text{O}$. *Phys. Rev. B* **2010**, *81*, No. 214437.
- (16) Georgiev, M.; Chamati, H. Magnetic excitations in molecular magnets with complex bridges: The tetrahedral molecule $\text{Ni}_4\text{Mo}_{12}$. *Eur. Phys. J. B* **2019**, *92*, No. 93.
- (17) Georgiev, M.; Chamati, H. Magnetization steps in the molecular magnet $\text{Ni}_4\text{Mo}_{12}$ revealed by complex exchange bridges. *Phys. Rev. B* **2020**, *101*, No. 094427.
- (18) Ray, M.; Yap, G. P.; Rheingold, A. L.; Borovik, A. S. Synthesis and characterization of a trigonal monopyramidal nickel(II) complex. *J. Chem. Soc., Chem. Commun.* **1995**, *17*, 1777–1778.
- (19) Kubica, A.; Kowalewski, J.; Kruk, D.; Odelius, M. Zero-field splitting in nickel(II) complexes: A comparison of DFT and multi-configurational wavefunction calculations. *J. Chem. Phys.* **2013**, *138*, No. 064304.
- (20) Gruđen-Pavlović, M.; Perić, M.; Zlatar, M.; García-Fernández, P. Theoretical study of the magnetic anisotropy and magnetic tunnelling in mononuclear Ni(II) complexes with potential molecular magnet behavior. *Chem. Sci.* **2014**, *5*, 1453–1462.
- (21) Singh, S. K.; Gupta, T.; Badkur, P.; Rajaraman, G. Magnetic Anisotropy of Mononuclear Ni^{II} Complexes: On the Importance of Structural Diversity and the Structural Distortions. *Chem. - Eur. J.* **2014**, *20*, 10305–10313.
- (22) Schulte, K. A.; Vignesh, K. R.; Dunbar, K. R. Effects of coordination sphere on unusually large zero field splitting and slow magnetic relaxation in trigonally symmetric molecules. *Chem. Sci.* **2018**, *9*, 9018–9026.
- (23) Rudowicz, C.; Gnutek, P.; Açıkgöz, M.; Verissimo-Alves, M.; Ślusarski, T. In *Semiempirical and DFT/Ab Initio Modeling of ZFS for Nickel(II) Complexes Exhibiting Very Large ZFS*, Third Joint Conference of Asia-Pacific EPR/ESR Society and Inter. EPR (ESR) Society (IES); Brisbane, Australia; Invited Talk, 2018.
- (24) Wojnar, M. K.; Laorenza, D. W.; Schaller, R. D.; Freedman, D. E. Nickel(II) Metal Complexes as Optically Addressable Qubit Candidates. *J. Am. Chem. Soc.* **2020**, *142*, 14826–14830.
- (25) Georgiev, M.; Chamati, H. Fine Structure and the Huge Zero-Field Splitting in Ni²⁺ Complexes. *Molecules* **2022**, *27*, No. 8887.
- (26) Charron, G.; Bellot, F.; Cisnetti, F.; Pelosi, G.; Rebilly, J.-N.; Rivière, E.; Barra, A.-L.; Mallah, T.; Polcar, C. Glycoligands Tuning the Magnetic Anisotropy of Ni^{II} Complexes. *Chem. - Eur. J.* **2007**, *13*, 2774–2782.
- (27) Suaud, N.; Rogez, G.; Rebilly, J.-N.; Bouammali, M.-A.; Guihéry, N.; Barra, A.-L.; Mallah, T. Playing with Magnetic Anisotropy in Hexacoordinated Mononuclear Ni(II) Complexes, An Interplay Between Symmetry and Geometry. *Appl. Magn. Reson.* **2020**, *51*, 1215–1231.
- (28) Campanella, A. J.; Ozvat, T. M.; Zadrozny, J. M. Ligand design of zero-field splitting in trigonal prismatic Ni(II) cage complexes. *Dalton Trans.* **2022**, *51*, 3341–3348.
- (29) Rogez, G.; Rebilly, J.-N.; Barra, A.-L.; Sorace, L.; Blondin, G.; Kirchner, N.; Duran, M.; van Slageren, J.; Parsons, S.; Ricard, L.; Marvilliers, A.; Mallah, T. Very Large Ising-Type Magnetic Anisotropy in a Mononuclear Ni^{II} Complex. *Angew. Chem.* **2005**, *117*, 1910–1913.
- (30) Reczyński, M.; Akaki, M.; Fukuda, T.; Sawada, Y.; Nishii, K.; Hagiwara, M.; Nitek, W.; Sieklucka, B.; Nowicka, B. Hepta-coordinated Ni(II) assemblies - structure and magnetic studies. *Dalton Trans.* **2021**, *50*, 5251–5261.
- (31) Chen, S.-Y.; Cui, H.-H.; Zhang, Y.-Q.; Wang, Z.; Ouyang, Z.-W.; Chen, L.; Chen, X.-T.; Yan, H.; Xue, Z.-L. Magnetic anisotropy and relaxation behavior of six-coordinate tris(pivalato)-Co(II) and -Ni(II) complexes. *Dalton Trans.* **2018**, *47*, 10162–10171.
- (32) Rebilly, J.-N.; Charron, G.; Rivière, E.; Guillot, R.; Barra, A.-L.; Serrano, M.; van Slageren, J.; Mallah, T. Large Magnetic Anisotropy in Pentacoordinate Ni^{II} Complexes. *Chem. - Eur. J.* **2008**, *14*, 1169–1177.
- (33) Costes, J.-P.; Maurice, R.; Vendier, L. Pentacoordinate Ni^{II} Complexes: Preparation, Magnetic Measurements, and Ab Initio Calculations of the Magnetic Anisotropy Terms. *Chem. - Eur. J.* **2012**, *18*, 4031–4040.
- (34) Jiang, S.-D.; Maganas, D.; Levesanos, N.; Ferentinos, E.; Haas, S.; Thirunavukkuarasu, K.; Krzystek, J.; Dressel, M.; Bogani, L.; Neese, F.; Kyritsis, P. Direct Observation of Very Large Zero-Field Splitting in a Tetrahedral Ni^{II}Se₄ Coordination Complex. *J. Am. Chem. Soc.* **2015**, *137*, 12923–12928.
- (35) Ruamps, R.; Maurice, R.; Batchelor, L.; Boggio-Pasqua, M.; Guillot, R.; Barra, A. L.; Liu, J.; Bendeif, E.-E.; Pillet, S.; Hill, S.; Mallah, T.; Guihéry, N. Giant Ising-Type Magnetic Anisotropy in Trigonal Bipyramidal Ni(II) Complexes: Experiment and Theory. *J. Am. Chem. Soc.* **2013**, *135*, 3017–3026.
- (36) Gómez-Coca, S.; Cremades, E.; Aliaga-Alcalde, N.; Ruiz, E. Huge Magnetic Anisotropy in a Trigonal-Pyramidal Nickel(II) Complex. *Inorg. Chem.* **2014**, *53*, 676–678.
- (37) Marriott, K. E. R.; Bhaskaran, L.; Wilson, C.; Medarde, M.; Ochsenbein, S. T.; Hill, S.; Murrie, M. Pushing the limits of magnetic anisotropy in trigonal bipyramidal Ni(II). *Chem. Sci.* **2015**, *6*, 6823–6828.
- (38) Rudowicz, C.; Açıkgöz, M.; Gnutek, P. Superposition model analysis of nickel(II) ions in trigonal bipyramidal complexes exhibiting huge zero field splitting (aka ‘giant magnetic anisotropy’). *J. Magn. Mater.* **2017**, *434*, 56–61.
- (39) Widener, C.; Bone, A.; Ozerov, M.; Richardson, R.; Lu, Z.; Thirunavukkuarasu, K.; Smirnov, D.; Chen, X.-T.; Xue, Z.-L. Direct Observation of Magnetic Transitions in a Nickel(II) Complex with Large Anisotropy. *Chin. J. Inorg. Chem.* **2020**, *36*, 1149–1156.
- (40) Craig, G. A.; Sarkar, A.; Woodall, C. H.; Hay, M. A.; Marriott, K. E. R.; Kamenev, K. V.; Moggach, S. A.; Brechin, E. K.; Parsons, S.; Rajaraman, G.; Murrie, M. Probing the origin of the giant magnetic anisotropy in trigonal bipyramidal Ni(II) under high pressure. *Chem. Sci.* **2018**, *9*, 1551–1559.
- (41) Yosida, K. *Theory of Magnetism*, Springer Series in Solid-State Sciences; Springer: Berlin; New York, 1996.
- (42) Abragam, A.; Bleaney, B. *Electron Paramagnetic Resonance of Transition Ions*; Oxford Classic Texts in the Physical Sciences; Oxford University Press: Oxford, 2012.

(43) Maurice, R.; Broer, R.; Guihéry, N.; de Graaf, C. Zero-Field Splitting in Transition Metal Complexes: Ab Initio Calculations, Effective Hamiltonians, Model Hamiltonians, and Crystal-Field Models. In *Handbook of Relativistic Quantum Chemistry*; Liu, W., Ed.; Springer Berlin Heidelberg: Berlin, Heidelberg, 2017; pp 765–796.

(44) Rudowicz, C. Concept of spin Hamiltonian, forms of zero field splitting and Electronic Zeeman Hamiltonians and relations between parameters used in EPR. A critical review. *Magn. Reson. Rev.* **1987**, *13*, 1–89. Rudowicz, C. Erratum. *Magn. Reson. Rev.* **1988**, *13*, 335.

(45) Georgiev, M.; Chamati, H. Magnetostructural Dependencies in $3d^2$ Systems: The Trigonal Bipyramidal V^{3+} Complex. *Phys. Status Solidi (b)* **2022**, *259*, No. 2100645.

(46) Sarkar, R.; Loos, P.-F.; Boggio-Pasqua, M.; Jacquemin, D. Assessing the Performances of CASPT2 and NEVPT2 for Vertical Excitation Energies. *J. Chem. Theory Comput.* **2022**, *18*, 2418–2436.

(47) Griffith, J. S. *The Theory of Transition-Metal Ions*; Cambridge University Press: Cambridge, 1961.

(48) Rudowicz, C.; Cecot, P.; Krasowski, M. Selection rules in electron magnetic resonance (EMR) spectroscopy and related techniques: Fundamentals and applications to modern case systems. *Phys. B: Condens. Matter* **2021**, *608*, No. 412863.